

An experimental and numerical study of nonlinear internal waves

Dominique P. Renouard

I.M.G./L.E.G.I. (U.J.F.-C.N.R.S.-I.N.P.G.), B.P. 53 X, 38041 Grenoble Cedex, France

Gunnar G. Tomasson and W. Kendall Melville^{a)}

R.M. Parsons Laboratory, Massachusetts Institute of Technology, Cambridge, Massachusetts 02139

(Received 12 December 1991; accepted 4 February 1993)

Nonlinear internal waves were measured on the large rotating platform at the Institut de Mécanique de Grenoble (I.M.G.). The experimental data complement the results presented in Renouard *et al.* [J. Fluid Mech. **177**, 381 (1987)] and support the assumption that the solitary Kelvin wave is accompanied by Poincaré waves. Based on the assumption of weak nonlinear, dispersive, and rotational effects, governing equations of the Boussinesq type are derived to model the evolution of an initial disturbance in a two-layer rotating fluid. The numerical study is based on these equations which are analogous to the Boussinesq equations of shallow-water theory and are not constrained to almost unidirectional propagation. Comparison of numerical solutions of the equations and experimental results are very good for moderately nonlinear conditions. These results provide supporting evidence for the resonant interaction of nonlinear Kelvin waves and linear Poincaré waves, as described by Melville *et al.* [J. Fluid Mech. **206**, 1 (1989)].

I. INTRODUCTION

In the oceans, as well as in large lakes, long internal waves are often both nonlinear and influenced by rotation. Without rotation, the balance of nonlinearity and dispersion leads to the formation of permanent waves which are either cnoidal or solitary waves satisfying the Korteweg-de Vries (KdV) equation. Such waves have been extensively studied both in homogeneous and stratified fluids. But as rotation is introduced some significant differences appear. Thus Renouard *et al.*¹ studying the properties of internal solitary Kelvin waves in a rotating channel (cf. Fig. 1 for notations) observed that, along the right-hand side of the channel, as well as in any plane parallel to the channel walls, the leading wave has a sech^2 profile, and that its celerity is independent of the distance to the wall, i.e., the front appears to be moving as a whole, with a phase speed fixed by the amplitude at the right-hand wall. For the ratios of Rossby radius to channel width, R/W , used in their experiments, [0.15, 0.43], the amplitude decreased exponentially with distance from the wall, the decay scale being $k=f/c_0=1/R$, where f is the Coriolis parameter, and c_0 the internal wave phase speed. Moreover, as in Maxworthy,² they noticed a strong curvature of the wave front. Although the initial conditions were clearly two dimensional, the wave, which was first generated with a horizontal crest perpendicular to the walls, changed its shape as it propagated along the channel, and, at some distance downstream, reached what appeared to be a stable shape, characterized by a strong curvature backwards. They suggested that the cause of the curvature, which appeared to be independent of the ratio between the layer thicknesses,

was likely to be either nonlinear or viscous effects. The leading wave was followed by a train of waves of smaller amplitude.

The experimental results suggested several theoretical and numerical studies. The first attempt to describe analytically such nonlinear waves in a channel was made by Grimshaw,³ who distinguished a "strong rotation" case (internal Rossby radius, at most, comparable to the wavelength), from a "weak rotation" case (internal Rossby radius much larger than the wavelength), but he could not account for the crest curvature in the absence of dissipation, in a channel of finite width. Independently, Germain and Renouard⁴ provided a uniform analytical framework for the study of all possible permanent progressive long waves in a rotating fluid.

To model the experiments, Katsis and Akylas⁵ used an informal derivation of the rotation modified Kadomstev-Petviashvili (KP) equation first derived by Grimshaw³ for the "weak rotation" case, and made some numerical computations. They were able to qualitatively reproduce most of the features appearing in the experiments, including the crest curvature, and suggested that, besides the viscous damping, the wave curvature was possible because of a slow attenuation of the wave as it propagated along the channel, but they did not relate such a decay to the small-amplitude waves that they observed behind the main curved disturbance. Both Grimshaw³ and Katsis and Akylas⁵ mentioned that there is a constraint on the KP equation which requires that the "mass" of the solution be proportional to $\exp(-y/R)$ at all times.

Melville *et al.*⁶ considered the evolution of weakly nonlinear dispersive long waves in a rotating channel. They showed that weakly nonlinear Kelvin waves may be unstable to a direct nonlinear resonance with the linear Poincaré modes of the channel. Thus the curvature of the wave front

^{a)}Present address: Scripps Institution of Oceanography, University of California, San Diego, La Jolla, California 92093-0213.

as well as the decay of the leading wave amplitude may be attributable to the Poincaré waves generated by the resonance. Later Grimshaw and Melville⁷ reconsidered the derivation of the rotation modified KP equation and its integral constraints, and showed that, in general, it is not permissible to assume that solutions to the rotation modified KP equation derived by Grimshaw³ are locally confined, and that there are Poincaré waves radiated behind the main part of the solution. More recently, Grimshaw and Tang⁸ also showed that any solitarylike wave must be accompanied by trailing Poincaré waves, so that any localized initial disturbance will evolve into a solitarylike wave with a curved wave front. They found that, as the effect of rotation increases, the extent of the wave curvature and the amplitude of the trailing Poincaré waves both increase.

While the role of the Poincaré waves which are generated by nonlinear waves in a rotating system have been investigated in a series of theoretical and numerical papers, only qualitative comparisons with the available experimental results have been possible. This has been due in part to the fact that asymptotic theories based on the KP equation and related equations which represent almost unidirectional propagation are unable to adequately model arbitrary initial conditions. This is related to the integral constraints described above. In this paper we present an experimental and numerical study of the evolution of an initial disturbance in a two-layer rotating fluid. The numerical study is based on the more general formulation of Tomasson and Melville⁹ which is analogous to the Boussinesq equations of shallow-water theory and is not constrained to almost unidirectional propagation. Initial conditions which can be reasonably generated in the experiments are faithfully represented in the numerical solutions.

II. EXPERIMENTAL SETUP

The experiments were conducted in the Coriolis Laboratory of the Institut de Mécanique de Grenoble. We used a channel, 9 m long, 2 m wide and 0.6 m deep, with a lighter upper layer of fresh water, and a denser lower layer of salt water. Figure 1 indicates the notation used. All the experiments were run with a lower layer 0.26 m thick, an upper layer 0.04 m thick, and a fractional density difference $\Delta\rho/\rho = O(0.01)$. For this set of experiments, the period of the platform rotation varied between 110 and 1000 sec, to give internal Rossby radii of deformation in the range $0.55 \text{ m} \leq R \leq 5.51 \text{ m}$, with dimensionless Rossby radii: $0.27 \leq R/W \leq 2.78$.

The channel was equipped with a dam at the upstream end, so that it was possible to have a thicker upper layer on one side of the dam. We denote by Δh the difference in thickness of the upper layers across the dam. This was usually set to 2 cm. By lifting the dam the light water behind the dam was released, and generated a wave train which propagated downstream. We chose Δh so that, without rotation, there would be only one solitary wave.

The interface height variations with time were recorded by interface followers at various locations. These

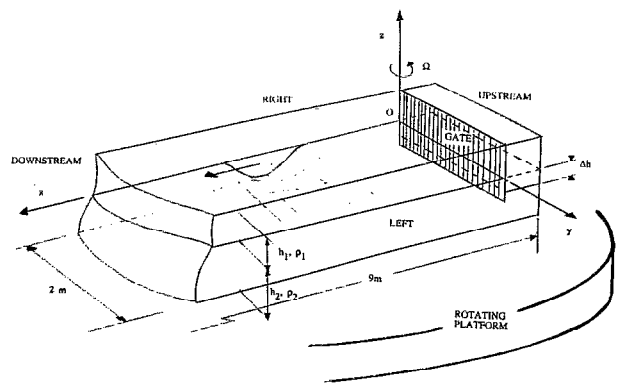


FIG. 1. Sketch of the notations used for the (9×2×0.6 m) channel built on the 14 m diam rotating platform and equipped with an internal wave generator.

probes are electronically directed to follow the movements of a layer of a given conductivity with great accuracy. The principle of these recorders is to measure the conductivity of a given reference layer, and to compare it with a chosen reference conductivity. With such an interface follower, we are able to follow the reference layer with an accuracy of 0.1 mm in height, and a response time of about 0.5 sec. Six such interface followers were used in these experiments. The probes were always following a layer very close to the inflection point of the interface profile. Thus the effects of the diffused interface can be minimized in the comparisons between the experiments and the computations.

III. NUMERICAL MODEL

We consider the motion of a two-layer fluid confined to a channel rotating on an f plane, i.e., with a constant Coriolis parameter. The fluid is assumed incompressible and inviscid, thus neglecting frictional effects at the channel walls, bottom, and at the interface between the two fluids. Furthermore, a rigid lid approximation is made, neglecting the barotropic surface-wave mode and looking only at the evolution of the baroclinic internal wave mode. The x axis is taken to be along the channel, the y axis across the channel and the z axis in the vertical direction, positive upwards. The fluid layers have constant densities ρ_1 and ρ_2 and depths h_1 and h_2 , with the interface between the fluid layers at the equilibrium position $z=0$. Following a derivation similar to that given by Tomasson and Melville⁹ for the corresponding single-layer case (the details of both derivations are given by Tomasson¹⁰), we obtain the Boussinesq momentum equations for the upper layer:

$$U_t^{(1)} + \alpha U^{(1)} U_x^{(1)} + \alpha \gamma V^{(1)} U_y^{(1)} - \epsilon V^{(1)} + \frac{1}{\rho_1} \bar{P}_x^{(2)} - \frac{1}{\rho_1} \eta_x - \beta \frac{h_1^2}{3} (U_{xxt}^{(1)} + \gamma U_{yyt}^{(1)}) = O(\beta^2), \quad (1)$$

$$\gamma V_t^{(1)} + \alpha \gamma U^{(1)} V_x^{(1)} + \alpha \gamma^2 V^{(1)} V_y^{(1)} + \epsilon U^{(1)} + \frac{\gamma}{\rho_1} \bar{p}_y^{(2)} - \frac{\gamma}{\rho_1} \eta_y - \beta \gamma \frac{h_1^2}{3} (V_{xxt}^{(1)} + \gamma V_{yyt}^{(1)}) = O(\beta^2); \quad (2)$$

and those for the lower layer

$$U_t^{(2)} + \alpha U^{(2)} U_x^{(2)} + \alpha \gamma V^{(2)} U_y^{(2)} - \epsilon V^{(2)} + \frac{1}{\rho_2} \bar{p}_x^{(1)} + \frac{1}{\rho_2} \eta_x - \beta \frac{h_2^2}{3} (U_{xxt}^{(2)} + \gamma U_{yyt}^{(2)}) = O(\beta^2), \quad (3)$$

$$\gamma V_t^{(2)} + \alpha \gamma U^{(2)} V_x^{(2)} + \alpha \gamma^2 V^{(2)} V_y^{(2)} + \epsilon U^{(2)} + \frac{\gamma}{\rho_2} \bar{p}_y^{(1)} + \frac{\gamma}{\rho_2} \eta_y - \beta \gamma \frac{h_2^2}{3} (V_{xxt}^{(2)} + \gamma V_{yyt}^{(2)}) = O(\beta^2), \quad (4)$$

together with the continuity equation for the upper layer:

$$-\eta_t + [(h_1 - \alpha \eta) U^{(1)}]_x + \gamma [(h_1 - \alpha \eta) V^{(1)}]_y = O(\beta^2) \quad (5)$$

and that for the lower layer:

$$\eta_t + [(h_2 + \alpha \eta) U^{(2)}]_x + \gamma [(h_2 + \alpha \eta) V^{(2)}]_y = O(\beta^2). \quad (6)$$

Here $U^{(1,2)}$ and $V^{(1,2)}$ are the depth-averaged horizontal velocities in each layer, η is the interface displacement, and $\bar{p}^{(1,2)}$ are the dynamic pressures at the interface, i.e.,

$$\bar{p}^{(1,2)}(x, y, t) = p^{(1,2)}|_{z=\alpha \eta}, \quad (7)$$

where p is the dynamic pressure in the fluid, i.e., the fluid pressure after subtracting the hydrostatic pressure. The scaling used here is

$$x' = k^{-1} x, \quad (8)$$

$$y' = l^{-1} y, \quad (9)$$

$$z' = h_0 z, \quad (10)$$

$$U^{(1,2)} = \alpha c_0 U^{(1,2)}, \quad (11)$$

$$V^{(1,2)} = \alpha \sqrt{\gamma} c_0 V^{(1,2)}, \quad (12)$$

$$t' = \frac{1}{kc_0} t, \quad (13)$$

$$\eta' = \alpha h_0 \eta, \quad (14)$$

$$p' = \alpha \rho_0 c_0^2 p, \quad (15)$$

$$h'_{1,2} = h_0 h_{1,2}, \quad (16)$$

$$\rho'_{1,2} = \rho_0 \rho_{1,2}, \quad (17)$$

where primes denote the dimensional variables. Here, $h_0 = h'_1 h'_2 / (h'_1 + h'_2)$ is an equivalent single-layer depth for

the corresponding linear and hydrostatic problem, $c_0^2 = (\Delta \rho / \rho) g h_0$ is the linear phase speed of the internal waves, $\Delta \rho = \rho'_2 - \rho'_1$ is the density difference, and ρ_0 is a reference density. The parameters we have introduced are

$$\alpha = A / h_0, \quad (18)$$

$$\beta = (k h_0)^2, \quad (19)$$

$$\epsilon = (1 / k R) (l / k), \quad (20)$$

$$\gamma = (l / k)^2, \quad (21)$$

representing nonlinear, dispersive (nonhydrostatic), rotational, and transverse effects, respectively. Here A is a measure of the amplitude of the disturbance, k^{-1} and l^{-1} are typical length scales in the x and y directions, respectively, and $R = c_0 / f$ is the internal Rossby radius of deformation. The above equations are based on the assumption of weak nonlinear, dispersive, and rotational effects, i.e.,

$$\alpha = O(\beta) = O(\epsilon) \ll 1, \quad (22)$$

which is the appropriate scaling for the experimental results presented here.

To obtain one pair of momentum equations we take the difference between the momentum equations in the two layers, i.e., $\rho_2 \cdot (3) - \rho_1 \cdot (1)$ and $\rho_2 \cdot (4) - \rho_1 \cdot (2)$. We assume that:

$$\Delta \rho / \rho \ll \beta, \quad (23)$$

which is an appropriate assumption for the experimental results presented here, and require that the mass fluxes in the two layers balance in the x and y directions independently, which gives

$$(h_1 - \alpha \eta) (U^{(1)}, V^{(1)}) = - (h_2 + \alpha \eta) (U^{(2)}, V^{(2)}), \quad (24)$$

which is the case for the lowest-order, linear, and hydrostatic problem. After using the appropriate matching conditions at the interface between the two layers, the following set of Boussinesq equations is obtained:

$$\eta_t + U_x + \gamma V_y = O(\beta^2), \quad (25)$$

$$U_t + \eta_x - \epsilon V + \alpha \left(\frac{1}{h_2} - \frac{1}{h_1} \right) [2UU_x + \gamma(VU)_y - \eta U_t] - \beta \frac{h_1 h_2}{3} (U_{xxt} + \gamma V_{yyt}) = O(\beta^2), \quad (26)$$

$$\gamma V_t + \gamma \eta_y + \epsilon U + \alpha \gamma \left(\frac{1}{h_2} - \frac{1}{h_1} \right) [(UV)_x + 2\gamma VV_y - \eta V_t] - \beta \gamma \frac{h_1 h_2}{3} (U_{xxt} + \gamma V_{yyt}) = O(\beta^2), \quad (27)$$

with the side-wall boundary conditions,

$$V = 0 \quad \text{at} \quad y = 0, W. \quad (28)$$

Here η is the interface displacement and U and V are the horizontal fluxes in the lower layer:

$$(U, V) = (h_2 + \alpha \eta) (U^{(2)}, V^{(2)}) \quad (29)$$

or equivalently, from (24), the negative fluxes in the upper layer. Equation (25) represents the continuity equation for either layer, whereas (26) and (27) come from the difference between the momentum equations in the two layers. We have also assumed that

$$\left(\frac{1}{h_2} - \frac{1}{h_1}\right) = O(1), \quad (30)$$

which is generally the case for the experimental results presented here.

In dimensional units these equations are

$$\eta_t + U_x + V_y = 0, \quad (31)$$

$$U_t + c_0^2 \eta_x - fV + \left(\frac{1}{h_2} - \frac{1}{h_1}\right) [2UU_x + (VU)_y - \eta U_t] - \frac{h_1 h_2}{3} (U_{xxt} + U_{yyt}) = 0, \quad (32)$$

$$V_t + c_0^2 \eta_y + fU + \left(\frac{1}{h_2} - \frac{1}{h_1}\right) [(UV)_x + 2VV_y - \eta V_t] - \frac{h_1 h_2}{3} (V_{xxt} + V_{yyt}) = 0, \quad (33)$$

with the side-wall boundary conditions

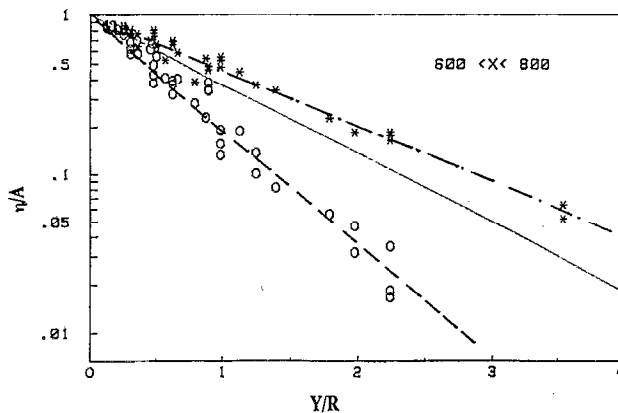
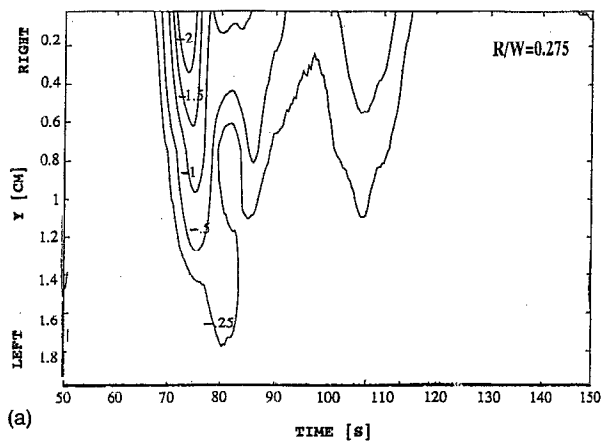


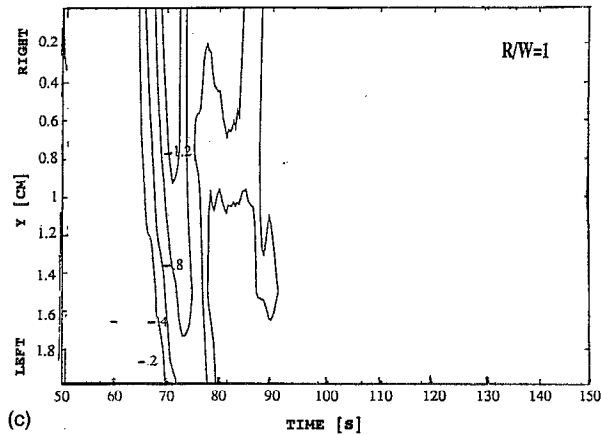
FIG. 2. Amplitude variations (η/A) vs (Y/R), in a plane perpendicular to the channel sides (\circ), and along the crest ($*$), for $6 \text{ m} < x < 8 \text{ m}$. The solid line plots $\exp(-y/R)$, the dotted lines, the decay scales computed from the data.

$$V = 0 \text{ at } y = 0, W, \quad (34)$$

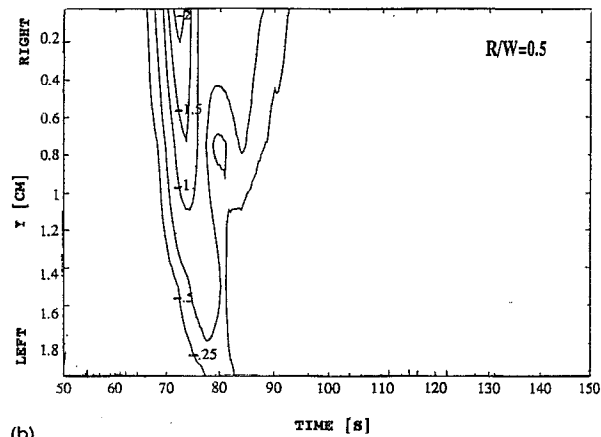
where, from now on, we have dropped the primes for convenience. Although slightly different from the corresponding single-layer equations derived by Tomasson and



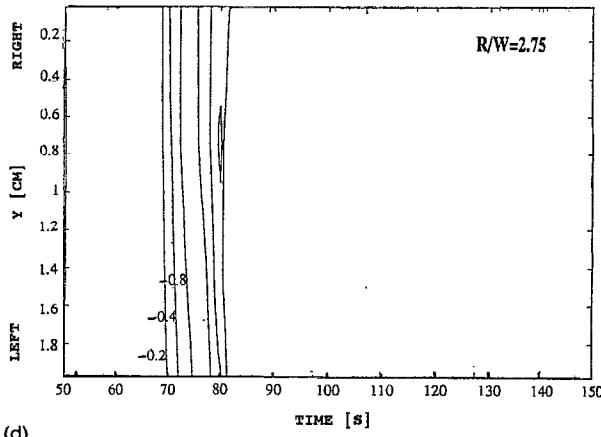
(a)



(c)

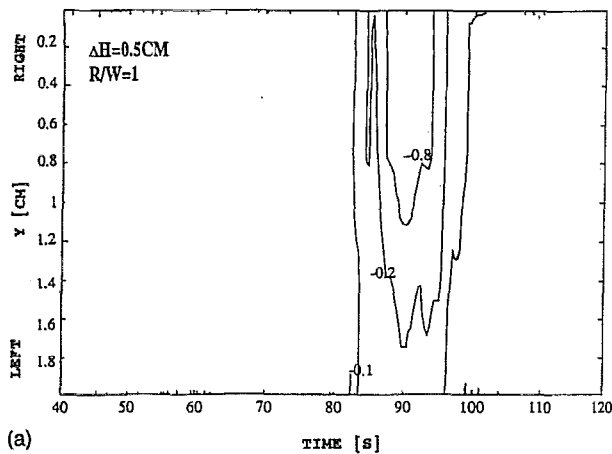


(b)

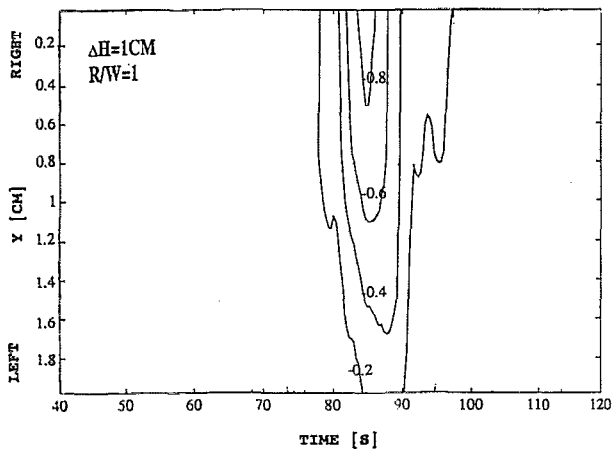


(d)

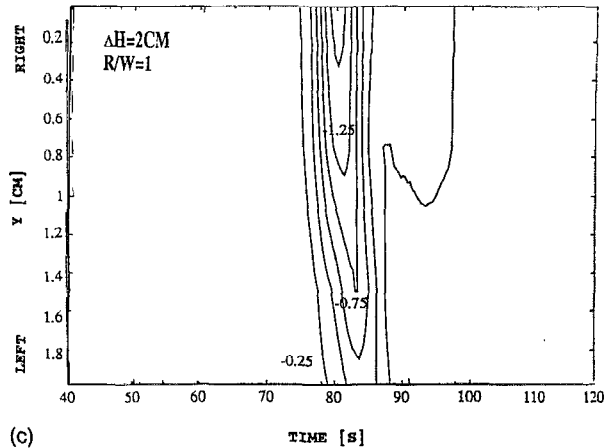
FIG. 3. Contour of interfacial displacement at $x=5 \text{ m}$ computed from the measured time series at four stations across the channel; $R/W=0.275$ (a), 0.5 (b), 1.0 (c), and 2.75 (d).



(a)



(b)



(c)

FIG. 4. Contour of the interfacial displacement computed from the measured time series at $x=5$ m, for three different initial conditions: $\Delta h=0.5$ cm (a), 1 cm (b), and 2 cm (c).

Melville,⁹ the important dynamics are the same. These equations are solved numerically using the scheme described by Tomasson and Melville.⁹

IV. EXPERIMENTAL RESULTS

We define k , the characteristic wavelength of the leading wave in the x direction as $k=(1/A) \times \int_0^\infty \eta(x-ct)d(x-ct)$, by using only the forward portion of the wave, in a method similar to that used by Koop and Butler.¹¹ For the experiments presented here, the ratio $2k/R$ was in the range $[0.11, 1.05]$ so that the conditions ranged from weak to strong rotation.

The downstream part of the leading wave is accurately described by the sech^2 profile. Having a large range of variation for R/W enabled us to obtain more accurate values for the decay scales across the channel. At $x=5$ m, the trace of the leading wave in a vertical plane perpendicular to the sides and passing through the maximum amplitude at the right-hand wall, A , is given by $A_t=A \times \exp(-0.82y/R)$, and the projection of the same crest on the same plane is described by $A_c=A \exp(-1.67y/R)$ (Fig. 2); the coefficients -0.82 and -1.67 being obtained by linear regression from the experimental data.

Because of the initial condition, the leading wave always starts with a wave front aligned with the y axis, but it immediately evolves toward a three-dimensional form. The increase of the phase shift across the channel with decreasing R/W is shown by contour plots generated from the

time series taken at four stations across the channel at $x=5$ m. These contour plots [Figs. 3(a)–3(d)] provide a space-time view of the disturbance. When the time delay is converted to a spatial phase shift based on the speed of propagation at the right-hand wall, we see that the spatial phase shift across the channel for small R/W may be as much as a meter. Looking at the evolution of the leading wave amplitude along the right-hand wall, we notice that it tends either to remain constant or even to increase along the first few meters and then decrease.

If we vary the initial layer thickness difference, from $\Delta h=0.5$ cm to 2 cm, but keep $R/W=1$, we can see at $x=5$

TABLE I. The parameters of the runs.

Fixed parameters		
Upper layer depth	h_1	4 cm
Lower layer depth	h_2	26 cm
Density difference	$\Delta\rho/\rho$	0.013
Coriolis parameter	f	0.0331 sec^{-1}
Linear wave speed	c_0	6.65 cm/sec
Rossby radius	R	2.0 m
Channel width	W	2.0 m
Variable parameters		
		run I run II run III run IV
Initial amplitude	a_0 (cm)	-0.5 -1.0 -1.5 -2.0

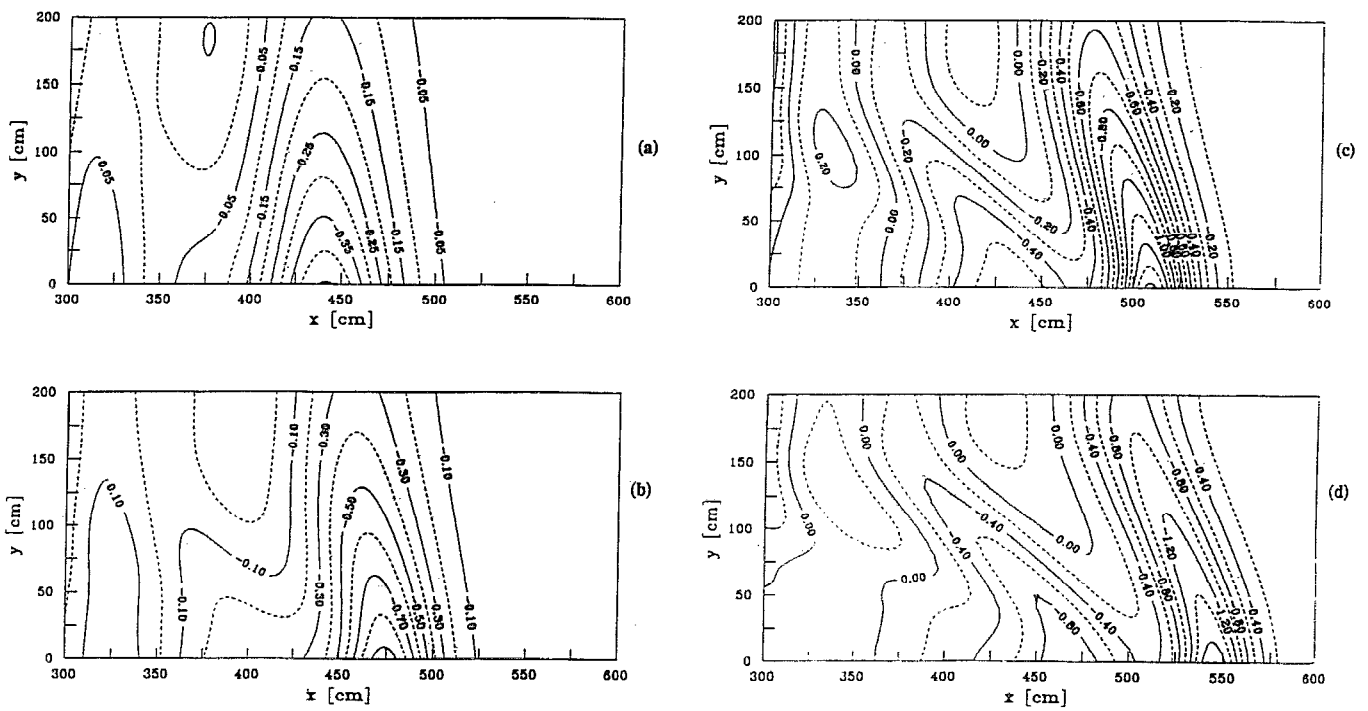


FIG. 5. Contour plots of the solution of Eqs. (31)–(33) for η at $t=65$ sec, corresponding approximately to the time the leading disturbance propagates past the stations at which time series are taken. (a) Run I, (b) run II, (c) run III, (d) run IV. Compare with Fig. 4.

m that for the smallest Δh , the leading crest is almost straight across the channel, while for $\Delta h > 1$ cm there is a significant phase shift (Fig. 4). Also, as expected, the celerity of the wave increases with increasing amplitude, i.e., for increasing Δh .

V. NUMERICAL RESULTS

The numerical model is used to compare with experimental data from four different runs, referred to here as runs I–IV. With the exception of the amplitudes of the initial disturbances, the parameters are the same for all the runs, and are listed in Table I. The initial disturbance in the numerical solution is chosen to simulate that of the experiments, i.e., a rectangular-shaped depression of the interface at the left (upstream) end of the channel with no associated flow velocity. The disturbance has no transverse variations and the sharp gradients are smoothed out by a tanh function.

In Fig. 5 a contour plot of the solution for η is given for all four runs at $t=65$ sec, which is approximately the time at which the leading disturbance propagates past the stations at which the time series are taken (see below). In all four runs, the leading disturbance is a Kelvin wave depression of the interface, followed by a tail of Poincaré waves. In run I very little nonlinear influence is visible. In the other three runs the effects of nonlinear evolution are clearly visible, with the crest of the leading wave curving backwards and the steepness and the speed of the waves increasing with increasing strength of the nonlinearities.

Also of interest is the appearance of a second wave behind the first, this second wave curving even further backwards and becoming stronger as the nonlinear effects become stronger.

A. Direct comparison of time series data

To compare directly with the experimental data, numerical and experimental time series of η taken at 5 m down the channel and at four stations across the channel, $y=2$, $y=50$, $y=125$, and $y=198$ cm, referred to here as stations 1–4, respectively, are compared. In Figs. 6–9 the numerical and experimental time series at the four stations are compared for all four runs. The time delay between the start of the data acquisition and the release of the initial disturbance in the experiments was not measured. Consequently, no time reference is available for the time series measurements, and a reference point in time had to be chosen for the numerical solutions. The reference point for the numerical solution is chosen such that the phase of the leading wave at station 1 (right-hand wall) matches that of the experimental wave for each of the runs.

Looking at the time series we see quite good agreement with the experimental data, particularly for runs II and III. The reason for the poorer agreement for run I may be the relatively small amplitudes of the waves, with the accuracy of the experimental measurements becoming an important factor, as can be clearly seen by the relatively small signal-to-noise ratio in Fig. 6. On the other hand, the reason for

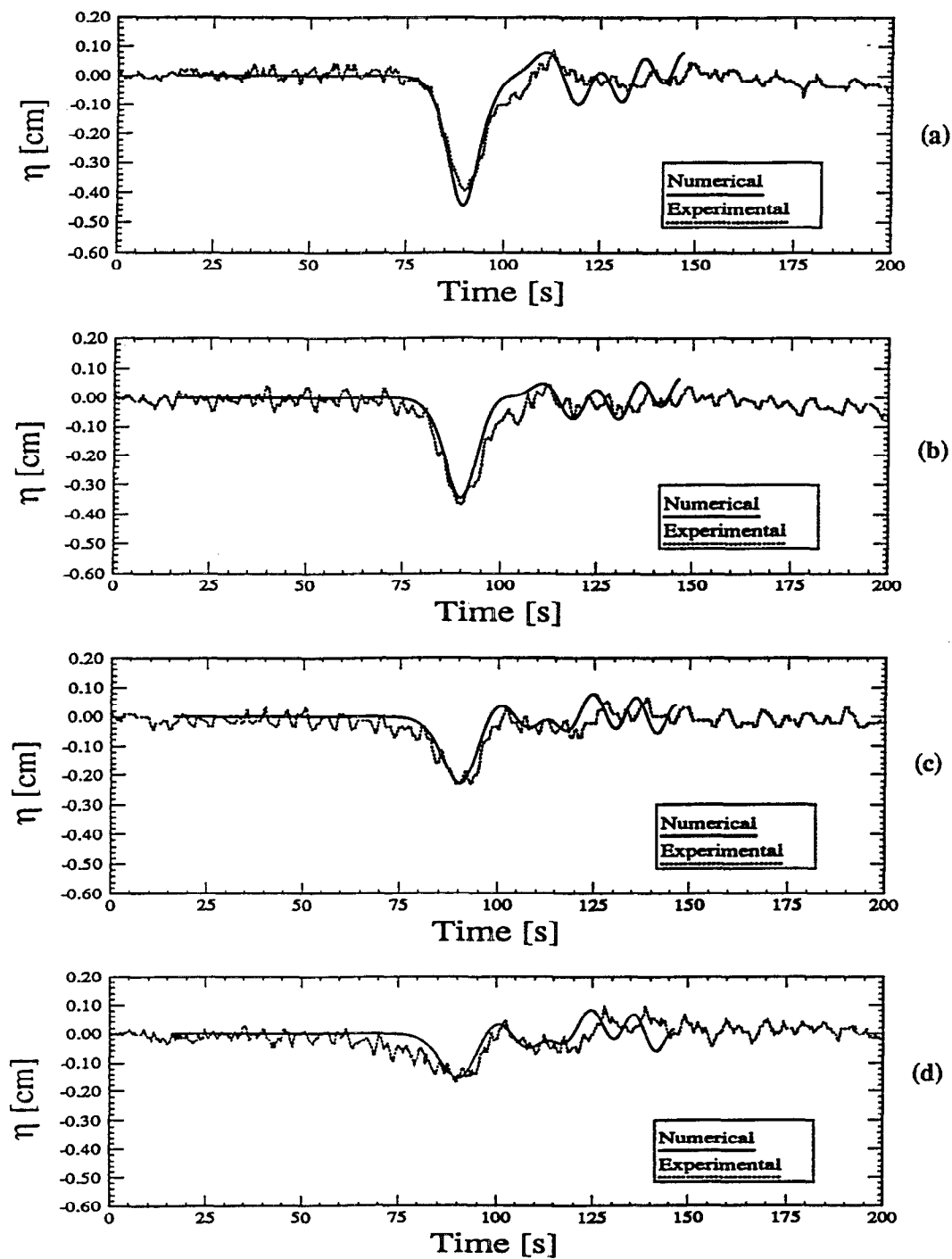


FIG. 6. The numerical and experimental time series for run I. (a) Station 1 ($x=5$ m, $y=2$ cm), (b) station 2 ($x=5$ m, $y=50$ cm), (c) station 3 ($x=5$ m, $y=125$ cm), and (d) station 4 ($x=5$ m, $y=198$ cm).

the poorer agreement for run IV may be the large amplitudes of the waves and consequently stronger nonlinearity, recalling that the Boussinesq equations are based on the assumption of weak nonlinearity. For these reasons, the following discussion will be largely based on runs II and III, i.e., the moderately nonlinear runs.

In general, the agreement for these two runs is very good, given the approximate nature of the equations and

their numerical solutions. The agreement in the phase of the leading wave at all stations is very good, meaning that the backward curvature of the crest, which is clearly visible in the time series, is well predicted by the numerical solutions. The good agreement in the tail of the leading wave is also striking, with the phase and frequency of the oscillations generally agreeing very well. Detailed analysis by Tomasson and Melville⁹ of similar trailing oscillations in the

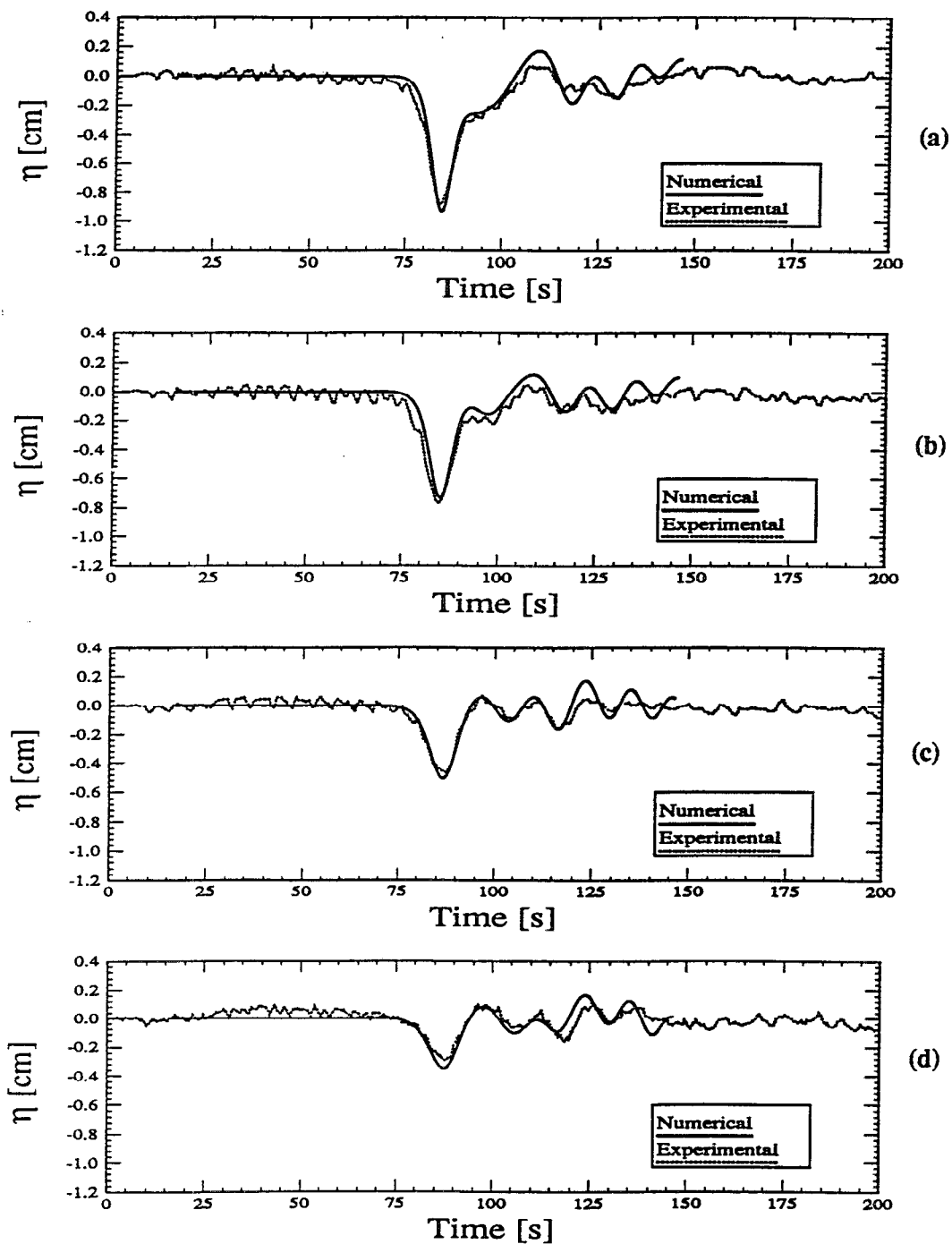


FIG. 7. The numerical and experimental time series for run II. (a) Station 1, (b) station 2, (c) station 3, and (d) station 4.

single-layer case have shown that they are partially due to resonantly generated Poincaré waves. The poorer agreement in the amplitude of the disturbances, especially in the stronger nonlinear cases, is most likely due to the neglect of frictional effects in the numerical model, with the numerical solutions consistently overpredicting the amplitudes.

B. Origin of the second wave

It is of some interest to try to understand the origin of the second wave appearing behind the leading wave. The

wave is quite clear both in the contour plots of the solution for η and in the time series of η . To investigate this, the numerical model was run with exactly the same parameters as in run III above, with the exception that the initial disturbance was moved away from the upstream end wall of the channel, as is shown in Fig. 10. Figure 11 shows a contour plot of the solution for η at $t=65$ sec [to be compared with Fig. 5(c) for run III], and Fig. 12 shows the time series of η at station 1, corresponding to Fig. 8(a) for run III. It is clear from these figures that the origin of the

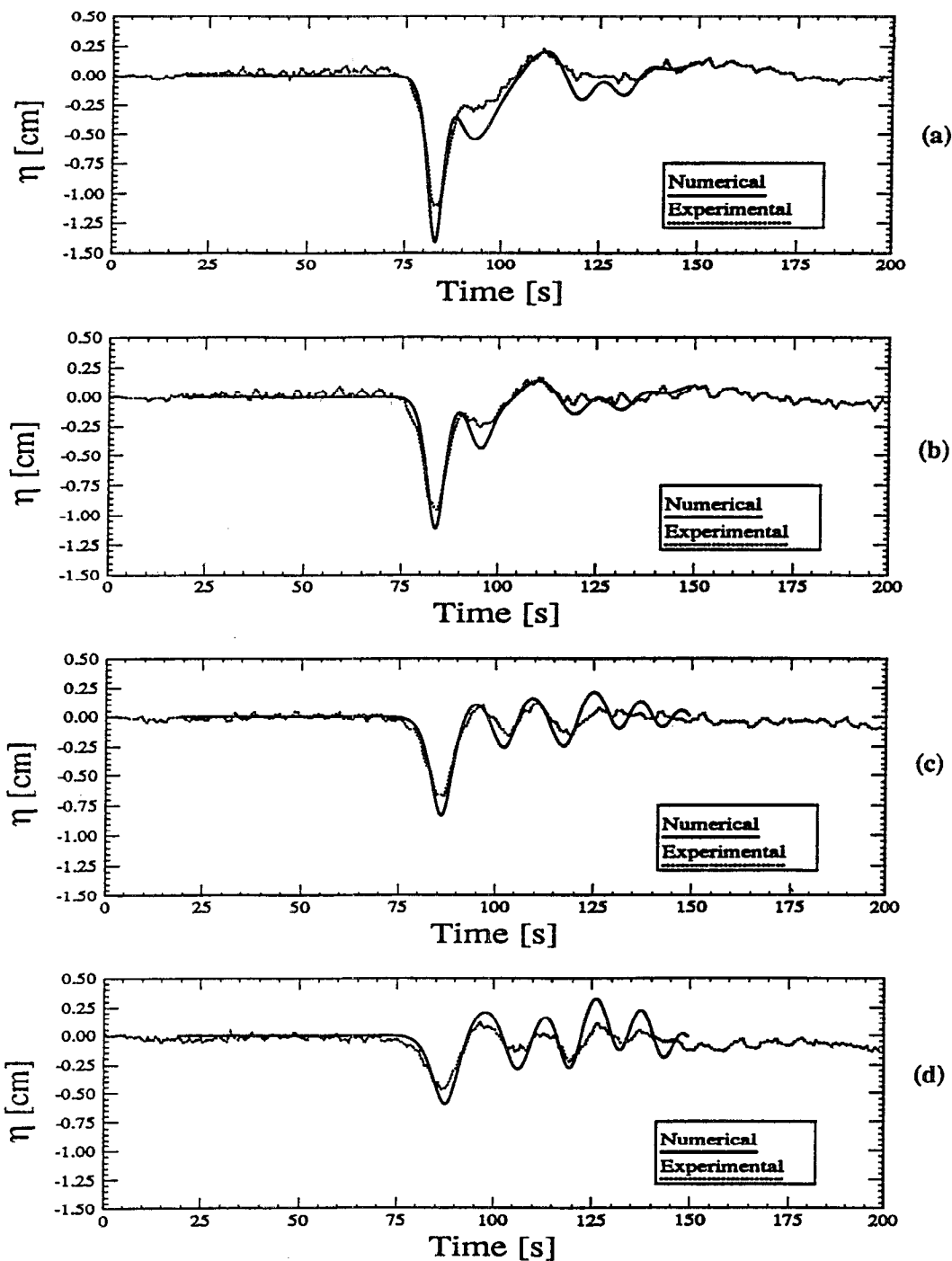


FIG. 8. The numerical and experimental time series for run III. (a) Station 1, (b) station 2, (c) station 3, and (d) station 4.

second wave is the adjustment and reflection of the initial disturbance from the upstream end wall. With the initial disturbance moved away from the upstream wall, the solution shows two well separated, but very similar waves, the second one resulting from the disturbance that travels down the channel to the left until reaching the upstream end wall and reflecting to follow the leading disturbance along the channel to the right. However, the second wave is contaminated by Poincaré waves generated by the lead-

ing wave, and thus has a slightly different structure. Also note that the leading wave is of smaller amplitude than before.

VI. DISCUSSION

In the experiments presented here the ratio of the characteristic wavelength to the Rossby radius was in the range $[0.11, 1.05]$ so that the rotation ranged from weak to strong.

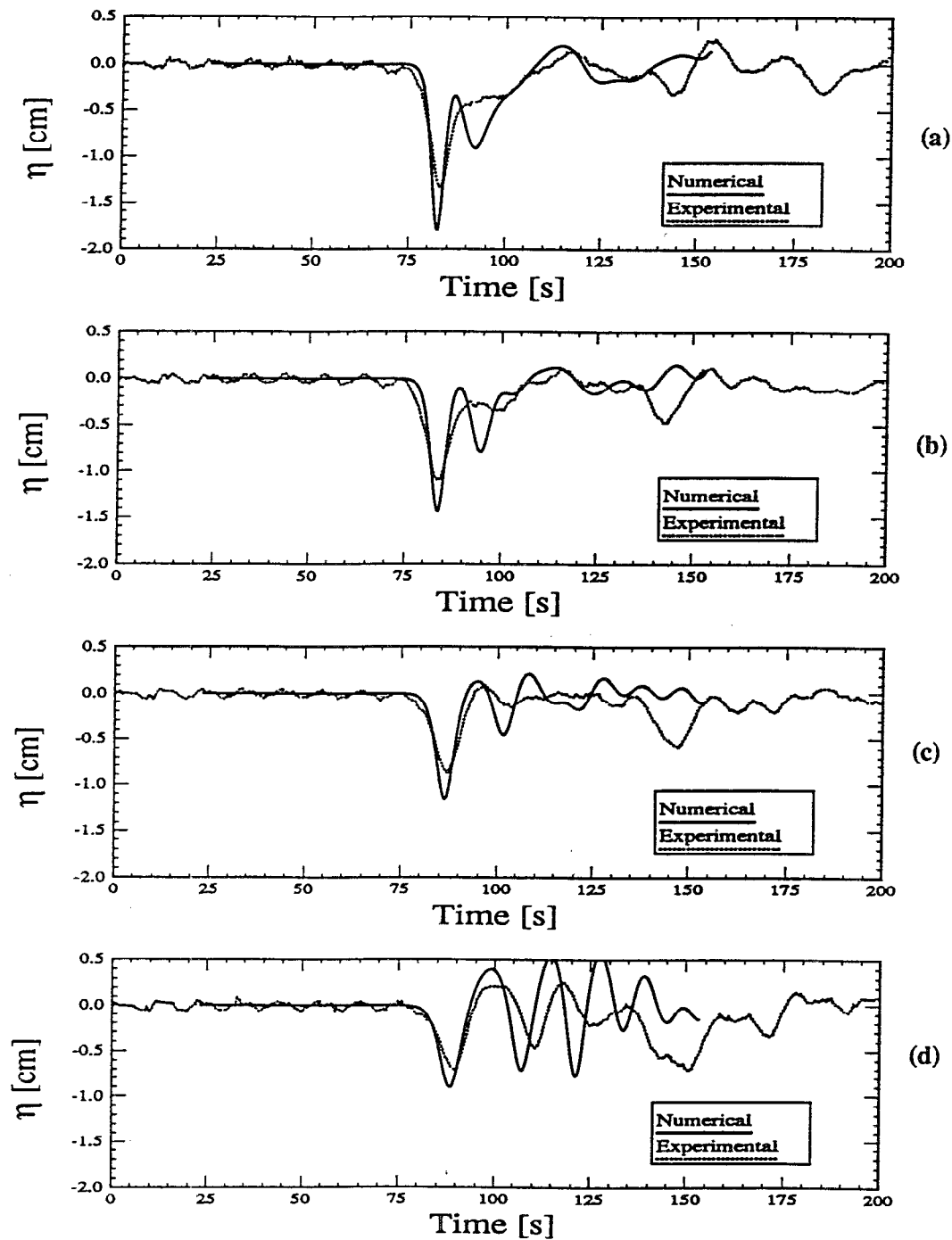


FIG. 9. The numerical and experimental time series for run IV. (a) Station 1, (b) station 2, (c) station 3, and (d) station 4.

The comparison between the experimental results and the numerical solutions based on the Boussinesq model is best for weak rotation, so we will restrict our conclusions to those cases. The basis of the quantitative comparison between the numerical and experimental results resides in Figs. 6–9. Given the difficulty of the experimental measurements, and the fact that the interface thickness is not equal to zero, it is remarkable that these comparisons show differences of less than 1 mm (or 10% based on the maxi-

um amplitude) in Figs. 7 and 8. These comparisons show that the Boussinesq model is able to accurately predict the evolution of nonlinear waves from initial data at rest; this has not been possible with previous formulations based on unidirectional propagation. This agreement supports the physical interpretation of the evolution of the disturbance based on the Boussinesq equations, and asymptotically on the simpler evolution equations. The primary conclusion is that the principal effects of weak rotation on the evolution

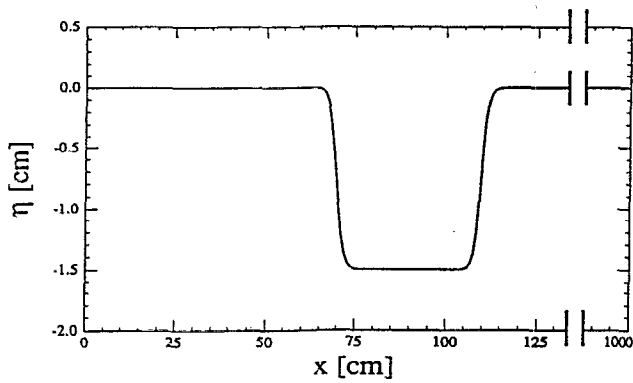


FIG. 10. The initial disturbance for η used to investigate the origin of the second wave. The upstream end of the channel is at $x=0$.

of weakly nonlinear long waves, which were first observed experimentally,^{2,1} and subsequently numerically,⁵ are due to the resonant generation of Poincaré waves as initially described by Melville *et al.*,⁶ and more recently by Tomasson and Melville.⁹ The experimental results also support the use of the Boussinesq equations for studies of geostrophic adjustment.

A secondary conclusion of the experimental and numerical results is that the second wave observed in many experiments may be due to the reflection of the leading wave which propagates toward the upstream end of the channel.

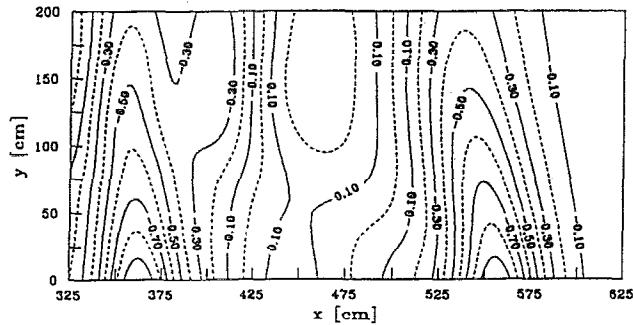


FIG. 11. A contour plot of the numerical solution of Eqs. (31)–(33) for η at $t=65$ sec from the run with the initial disturbance separated from the upstream end wall.

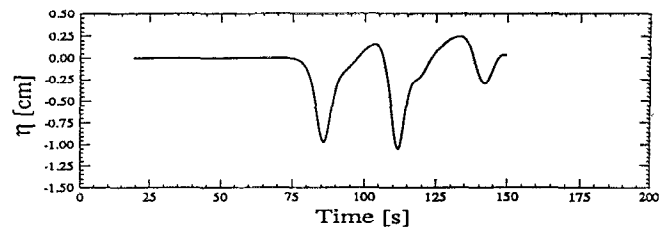


FIG. 12. Time series of η from the numerical solution for the initial disturbance separated from the upstream end wall.

ACKNOWLEDGMENTS

The authors are extremely grateful to X. Zhang, who helped perform the experiments, and did the initial data processing. They also wish to thank G. Chabert d'Hières for his support. DPR thanks Professors J. P. Germain and C. C. Mei for many interesting comments on these experimental results.

This work was supported both by C.N.R.S. and N.S.F. (International Programs) as part of a joint program, and by O.N.R. (Coastal Science).

¹D. Renouard, G. Chabert d'Hières, and X. Zhang, "An experimental study of strongly nonlinear waves in a rotating fluid," *J. Fluid Mech.* **177**, 381 (1987).

²T. Maxworthy, "Experiments on solitary internal Kelvin waves," *J. Fluid Mech.* **129**, 362 (1983).

³R. Grimshaw, "Evolution equations for weakly nonlinear, long internal waves," *Stud. Appl. Math.* **73**, 1 (1985).

⁴J. P. Germain and D. Renouard, "On permanent nonlinear waves in a rotating fluid," *Fluid Dyn. Res.* **7**, 263 (1991).

⁵C. Katsis and T. R. Akylas, "Solitary internal waves in a rotating channel: A numerical study," *Phys. Fluids* **30**, 297 (1987).

⁶W. K. Melville, G. G. Tomasson, and D. P. Renouard, "On the stability of Kelvin waves," *J. Fluid Mech.* **206**, 1 (1989).

⁷R. Grimshaw and W. K. Melville, "On the derivation of the modified Kadomstev–Petviashvili equation," *Stud. Appl. Math.* **80**, 183 (1989).

⁸R. Grimshaw and S. Tang, "The rotation modified Kadomstev–Petviashvili equation: An analytical and numerical study," *Stud. Appl. Math.* **83**, 223 (1990).

⁹G. G. Tomasson and W. K. Melville, "Geostrophic adjustment in a channel: Nonlinear and dispersive effects," *J. Fluid Mech.* **241**, 23 (1992).

¹⁰G. G. Tomasson, "Nonlinear waves in a channel; three dimensional and rotational effects," Sc.D. thesis, Massachusetts Institute of Technology, 1991.

¹¹C. G. Koop and G. Butler, "An investigation of internal solitary waves in a two-fluid system," *J. Fluid Mech.* **112**, 225 (1981).